actuators

MDPI

Article

Overview of the SmartX Wing Technology Integrator

Roeland De Breuker *, Tigran Mkhoyan, Nakash Nazeer, Vincent Stuber, Xuerui Wang, Iren Mkhoyan, Roger Groves, Sybrand van der Zwaag and Jurij Sodja

Department of Aerospace Structures and Materials, Faculty of Aerospace Engineering, Delft University of Technology, 2629 HS Delft, The Netherlands

* Correspondence: r.debreuker@tudelft.nl; Tel.: +31-15-278-56-27

Abstract: This article describes the challenges of integrating smart sensing, actuation, and control concepts into an over-sensed and over-actuated technology integrator. This technology integrator has more control inputs than the expected responses or outputs (over-actuated), and its every state is measured using more than one sensor system (over-sensed). The hardware integration platform is chosen to be a wind tunnel model of a low-speed aircraft wing such that it can be tested in a large university-level wind tunnel. This hardware technology integrator is designed for multiple objectives. The nature of these objectives is aerodynamic, structural, and aeroelastic, or, more specifically; drag reduction, static and dynamics loads control, aeroelastic stability control, and lift control. Enabling technologies, such as morphing, piezoelectric actuation and sensing, and fibre-optic sensing are selected to fulfil the mentioned objectives. The technology integration challenges are morphing, actuation integration, sensor integration, software and data integration, and control system integration. The built demonstrator shows the intended level of technology integration.

Keywords: autonomous wing; over-actuated wing; over-sensed wing; technology demonstrator

Citation: De Breuker, R.; Mkhoyan, T.; Nazeer, N.; Stuber, V.; Wang, X; Mkhoyan, I.; Groves, R.; van der Zwaag, S.; Sodja, J. Overview of the SmartX Wing Technology Integrator. *Actuators* **2022**, *11*, 302. https://doi.org/10.3390/act11100302

Academic Editor: Ronald M. Barrett

Received: 1 September 2022
Accepted: 19 October 2022
Published: 20 October 2022

1. Introduction

Smart structures have been present since the dawn of aviation. The first heavier-than-air powered flight by the Wright brothers in 1903 was carried out with an aircraft that was able to twist morph its wings. Morphing was quite common in those pioneering years. However, aircraft became larger and heavier, and the wing loading increased. This necessitated the wings to become stiffer to carry the increased loads, and this increased stiffness prevented the wing from morphing. The separation of functionalities in aircraft wings was introduced, where the wing load-carrying structure was separated from the rigid wing movables, which enabled the wing's high-lift and rolling capabilities [1]. Only a handful of later morphing aircraft examples can be found, and they are mainly limited to experimental or military aircraft. Iconic examples are the F14 Tomcat and F111 Aardvark. However, since the 1980s, a renewed interest in smart structures for aviation has originated from the Active Flexible Wing (AFW), the Active Aeroelastic Wing (AAW), and the Aircraft Morphing and the Morphing Aircraft Structures programmes of the National Aeronautics and Space Administration (NASA) and the Defense Advanced Research Projects Agency (DARPA), amongst others [2–6]. On the civil aircraft side, the interest in smart structures for aviation has spiked in the European Union (EU) Framework Programmes (FP), more specifically FP5, FP6, FP7, and H2020. Much of the research in these programmes was focused on individual non-integrated morphing, actuation, or sensing concepts. These programmes focused on topics such as, but not limited to, morphing using compliant mechanisms [7], span and chord morphing mechanisms [8], or aircraft sensing methods [9]. Only occasionally did hardware demonstrators contain multiple actuation or sensing concepts. An example is the EU FP7 Smart Intelligent Aircraft Structures (SARISTU) project [10]. More examples are the X-HALE nonlinear aeroelastic flying platform developed by Cesnik and co-workers. They focused on shape control, manoeuvre and gust load control, and

control allocation [11,12]. A large-scale isolated wing [13] and half aircraft [14] wind tunnel model for load control was developed by Ricci and co-workers. They experimentally demonstrated load alleviation using multiple control surfaces. Distributed trailing edge control surface effects on a 2 m flexible wing were investigated experimentally in the wind tunnel at Washington University [15]. A closed-loop 2.1 m morphing wing wind tunnel test was performed at the National Research Council of Canada [16].

A multitude of review articles has been written about the application of smart structures for aeronautical applications [17–22]. These review articles conclude that smart aeronautical structures for civil applications will be used for performance improvements of an aircraft to enhance the greening of aviation. They also stipulate that an integrated, multidisciplinary approach is needed. However, they observe that, relative to the numerical investigations that have taken place, very little smart structures concepts have been tested in the lab, wind tunnel, or in flight. An integrated closed-loop over-sensed and over-actuated wing hardware technology integrator has not yet been investigated. This is the aim of the technology that is described in this paper.

A project called SmartX was started for this purpose at the Delft University of Techology, faculty of Aerospace Engineering, department of Aerospace Structures and Materials. The aim of this project is to investigate the feasibility of developing, manufacturing, and testing such a multi-objective technology integrator with integrated smart sensing, actuation, and control methodologies. The aim of this paper was to provide an overview of the idea behind this next step in the development and maturing of smart structures of aeronautical applications, the SmartX project, as well as how this idea is translated concretely into a hardware technology integrator. More detailed descriptions of the individual contributing technologies and the results of the hardware test campaigns will be published in follow-up articles.

The philosophy behind these multiple objectives that this wing is designed for is explained in Section 2. The individual technologies that have contributed to this technology integrator are explained in Section 3. The way these technologies are integrated in a closed-loop sense is described in Section 4. Initial results are shared and discussed in Section 5. Finally, the SmartX project overview is summarised in Section 6.

2. SmartX Philosophy

The main objective of the SmartX project is the integration of smart sensing, smart actuation, and smart control into one single hardware technology integrator meeting multi-objective purposes, defined below. The chosen integrator platform is a wing of a low-speed uninhabited aerial vehicle to be tested in the low-speed wind tunnels at the Delft University of Technology. The multiple objectives of the SmartX technology integrator are:

1. Drag reduction in cruise: the goal is to continuously optimise in real-time the wing shape during the cruise phase to constantly fly at minimum drag. This drag consists of two main components: (i) induced drag and (ii) friction drag. The shape of the wing is constantly adapted to generate a lift distribution that is close to elliptic to yield a constant downwash distribution and hence minimum induced drag. Secondly, the wing shape is adapted actively to increase the laminar boundary layer region over the wing surface, hence actively reducing the friction drag;
2. Load control: minimisation of dynamic and static flight loads will lead to a minimum structural mass to withstand the aerodynamic loads. Static flight loads are typically manoeuvre loads, while dynamic loads are gust loads. Static and quasi-static loads require low-frequency actuation, while gust loads require, depending on the gust length, high-frequency actuation. Hence, two types of (morphing) movables are necessary;
3. Aeroelastic stability control: the move towards aircraft structures of lower structural mass leads to more flexible wings. Such wings are more prone to aeroelastic instability such as flutter. Avoidance of flutter in a passive sense will lead to an increase in structural mass; hence the flutter phenomenon needs to be controlled in an active manner using the same control system that is used for gust loads control;

4. Lift control: in order to ensure that the aircraft lift always exceeds or is equal to its mass even in slow flight, the shape of the wing can be controlled automatically to provide high-lift capabilities.

The ultimate goal of the SmartX project is to quantify how much these four objectives can contribute simultaneously to a reduction in energy consumption on the aircraft level. Such a reduction in energy consumption is necessary to reduce the greenhouse gas emissions of an aircraft or to enable lower emission, but also lower energy density and energy carriers. An experimental quantification of energy consumption is rarely made on an individual technology level, and is even rarer on a technology integrator level.

The above-mentioned multiple objectives are comparable to the objectives of the NASA Variable Camber Continuous Trailing Edge Flap (VCCTEF) project [23]. The three main differences are that (i) the SmartX objectives are to be achieved fully autonomously, that (ii) the closed-loop control to achieve these objectives is demonstrated using a hardware technology integrator, and that (iii) the intended sensing, actuation, and control technologies to be used are different. The main advantage of the SmartX project is the demonstration of the next step in Technology Readiness Level (TRL) of smart concept integration, which is a critical step in the development and maturing of the next generation of smart aeronautical structures.

To achieve the multiple objectives that are described above, we need to integrate several smart technologies in the areas of sensing and actuation. The goal of each actuation and sensing concept is explained here and elaborated further in Section 3.

1. Slow morphing: Morphing is chosen as the actuation concept instead of the use of discrete control surfaces. The reason is aerodynamic efficiency due to the seamless spanwise and chordwise morphing deformations. The slow morphing concept in this project should be able to seamlessly change the wing camber and twist in a distributed fashion. The morphing control surface is located at the wing trailing edge and can exhibit large deflections, which in this paper means more than 20% of morphing flap length, at an operational quasi-steady frequency in the order of 0.1 Hz to 1 Hz;
2. Fast morphing: The fast morphing control surfaces are discrete tabs that are located at the very trailing edge of the slow morphing control surfaces. The tab deflections are an order of magnitude smaller than the slow morphing control surface deflections, but their operational frequency is one order of magnitude higher, up to 10 Hz. This frequency range stems from the gust frequency requirements as specified by the certification specifications [24];
3. Shape sensing: Knowledge of the wing and morphing control surfaces shape is needed to obtain the exact control setting. This information is needed for closed-loop control purposes. It suffices for conventional rigid and discrete control surfaces to find the actuator setting since it determines the remainder of the control system behaviour unambiguously. This is no longer the case for morphing control surfaces since they exhibit a continuous and flexible deformation that is influenced by the actuator setting, the aerodynamic loads, and the deflection of the neighbouring seamless control surfaces. Therefore, knowledge about both the transient and steady-state wing and morphing control surface shapes is necessary;
4. Boundary layer sensing: Knowledge of the state of the boundary layer is important for the shape control both for in-flight cruise shape optimisation and automated high-lift generation. Knowing whether the boundary layer is turbulent or laminar is important for cruise shape optimisation, while knowing whether the boundary layer is attached or separated is important in the case of automated high-lift. The flow sensing hardware must be integrated into the wing skin since it needs to be able to be operated in flight.

An overview of which technology is used for which purpose is given in Table 1.

Table 1. SmartX project objectives and related technologies.

	Drag Reduction	Load Control	Aeroelastic Stability Control	Lift Control
Slow morphing	✓	✓	-	✓
Fast morphing	-	✓	✓	-
Shape sensing	✓	-	-	✓
Boundary layer sensing	✓	-	-	✓

All of these interconnected technologies are to be realised on a wing with a span of 1800 mm and chord of 500 mm, yielding an aspect ratio of 7.2 since the wing is cantilevered at the root. The dimensions of the wing are chosen such that it would fit into the Open Jet Facility (OJF) wind tunnel of the Delft University of Technology, which has a square cross-section of 2850 mm by 2850 mm. The design loads for the wing are determined by the maximum flow velocity of the OJF of 35 m s^{-1}. The wing is constructed of carbon fibre composites. More details about the wind tunnel model design can be found in Ref. [25].

3. SmartX Enabling Technologies

This section details the technologies that are developed to achieve the goals that were introduced in Section 2.

3.1. Trailing Edge Slow Morphing

The slow morphing concept is a concept that cambers and twists the trailing edge of the wing in a frequency bandwidth of typically 0.1 Hz to 1 Hz. The SmartX slow morphing concept is based on the Translation Induced Camber (TRIC) concept that was developed at the Delft University of Technology [26]. The TRIC concept is a chordwise seamless morphing concept that exhibits large deformations and the associated blocked force but, although seamless, does not introduce locally large strains in the structure. This enables the use of off-the-shelf aerospace materials, which makes the morphing concept feasible and scalable for a wide range of aircraft classes.

The basic idea behind the TRIC concept is that the closed cell of a control surface is cut to reduce its torsional stiffness. The cut that was introduced is closed using a linear actuator. Therefore, the control surface can be moved without virtually any resistance from the skin while the actuator is moving, but the control surface closed-cell obtains the actuator stiffness once the actuator is locked. The idea behind the concept is shown in Figure 1. There, the slot in which the trailing edge skin can move in the chordwise direction can be observed. The relative motion of the trailing edge skin in the chordwise direction is ensured by the integrated linear actuator, which is located inside the wingbox. Each of the six morphing flaps is equipped with two actuators located at either side of the flap in the spanwise direction. The actuators are Volz DA 22-12-4112 servos selected for their high blocked force and position feedback capabilities, counting to 12 in total for all 6 modules. The cut-off frequency of the actuation module is identified to be ≈2.6 Hz (16.3 rad s^{-1}), and limited to a peak-to-peak amplitude of 25°. The TRIC concept actuation is added inside the wing box for demonstration purposes only. The actuation system can also be entirely

embedded inside the morphing flap itself. This would leave sufficient space inside the wing box to store fuel or other energy carriers.

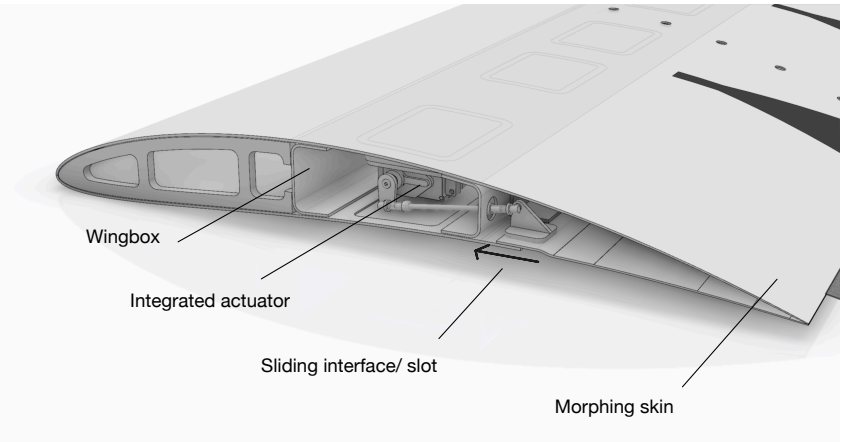

Figure 1. SmartX slow morphing concept: the trailing edge can seamlessly move up and down.

The SmartX hardware technology integrator is equipped with six trailing edge flaps that contain the TRIC concept. These trailing edge TRIC flaps cover the entire span of the wing and are equally spaced. The gap between each of the individual flaps is closed using a flexible elastomeric material to make the wing trailing edge entirely seamless both in chordwise (due to the morphing concept) and spanwise (due to the silicone material) directions. The flexible elastomeric skin has been optimised such that a balance is found between the desired tip flexibility and required actuator loads.

Within the intended bandwidth up to 1 HZ, the slow morphing concept can exhibit peak-to-peak trailing edge deflections up to 16 mm upwards and 14 mm downwards and deliver a blocked force, which is in the order of the applied loads that can be expected on a wing of the size of the SmartX hardware technology integrator. Given the speed regime of the envisioned wind tunnel of 10–20 m/s, the maximum static and dynamic loads are expected to be 50 N.

Variable skin stiffness in the form of skin thickness tailoring ensures that the trailing edge skin is sufficiently stiff to support the aerodynamic loads while it is flexible enough to allow for the required deformations. The variable skin thickness is made possible by making use of ply drops of a composite skin. This is needed to obtain a smooth outer surface while matching a prescribed target shape for the control surface. A fluid-structure interaction routine was used to determine the most optimal ply dropping sequence. More details about this procedure can be found in Mkhoyan et al. [25]. The result of the optimisation can be seen in Figure 2 for a single slow morphing module.

3.2. Trailing Edge Fast Morphing

Along the morphing trailing edge, 190 clustered piezoelectric bimorphs operating in the inverse piezoelectric mode (i.e., an applied voltage induces a displacement) are installed to provide additional fast response morphing capabilities to the wing. Figure 3 gives an overview of the bimorphs and how they were installed. Each bimorph was manufactured industrially and consisted of a Pernifer 45 substrate layer, with PZT-5A4 piezoelectric ceramics bonded to either side. The choice of these materials was made because they are well-known, proven technologies. The bimorphs have three free electrodes, one on either side and one connected to the Pernifer 45 substrate, making it able to connect the piezoelectric layers in parallel. The electrodes of 10 bimorphs were connected in parallel using solder, resulting in 3 wire connections per 10 bimorphs. This means that separate actuation can be performed on each set of 10 bimorphs. They are fixed in the trailing edge of the wing by filling the gap between the bimorphs and the top and bottom skins with epoxy resin, providing a free length outside the wing of about 35 mm. In total, 19 sets of

10 bimorphs are installed: 3 in the centre of each of the 6 sections, with an additional one at the very tip.

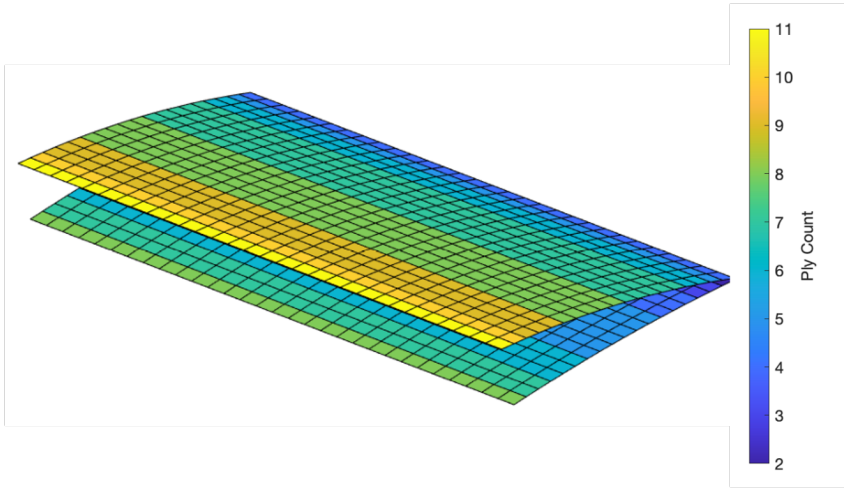

Figure 2. TRIC skin ply drop pattern (one layer has a thickness of 0.12 mm).

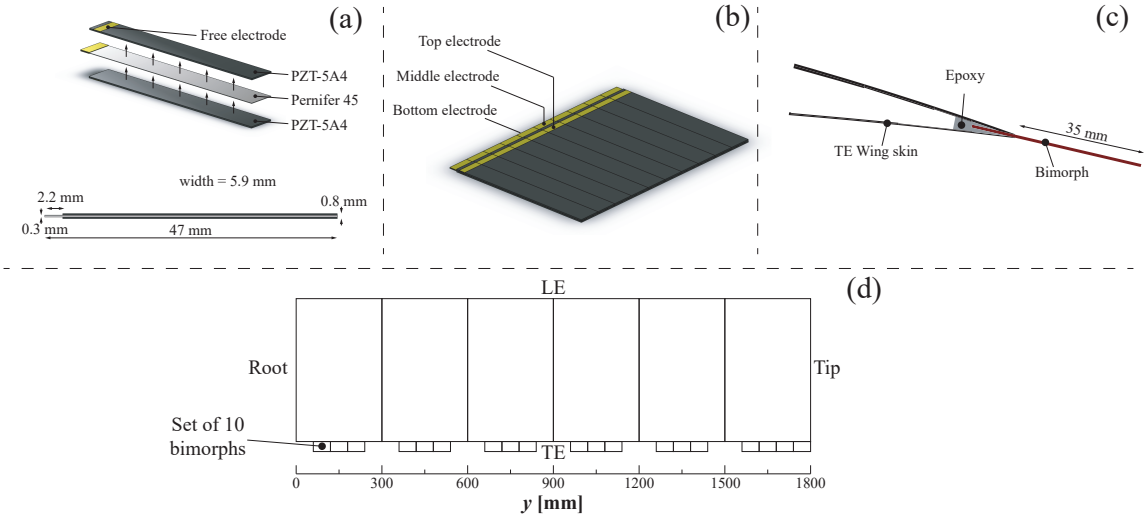

Figure 3. (**a**) Single piezoelectric bimorph. (**b**) Set of 10 bimorphs connected in parallel. (**c**) Cross-section of the trailing edge. (**d**) Distribution of the 19 sets of 10 bimorphs in the SmartX wing.

Figure 4 shows the circuit diagram connected to each set of 10 bimorphs. The inputs to the diagram are two drive signals, *Drive 1* and *Drive 2*, and one constant positive 200 V supply. The input drive signals are always 0 V or 5 V powering the switches, which are optical MOSFET switches. The input signals are directly coming from an Arduino controller. By powering *Drive1* or *Drive2* the bimorphs can be actuated up or down, while by powering none of the two, they are left in the neutral position. If for any reason both *Drive1* and *Drive2* are powered, they also keep their neutral position. The benefit of this circuit is that only one 200 V power supply is required to actuate the bimorphs, while the limitation is that only three settings can be realised: bend down, neutral, and bend up.

The response time of the circuit is about 2 ms. However, a more limiting factor is the amount of current the 200 V supply can provide. Whenever one set of 10 bimorphs is switched on, it draws a significant amount of current. The total amount of power required linearly scales with the number of sets switching simultaneously. The maximum power required is limited by limiting the maximum operating frequency to 50 Hz, yielding a system response time of 20 ms. Using frequencies up until 50 Hz, the bimorphs are able to

obtain a peak-to-peak tip deflection of about 2.50 mm (+1.25 mm bend up and −1.25 mm bend down).

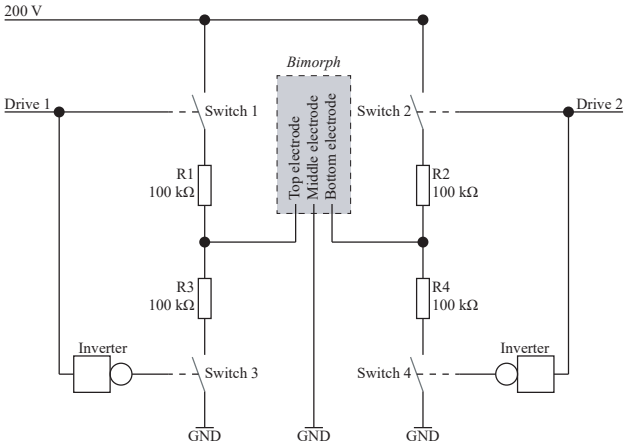

Figure 4. Circuit diagram powering 1 set of 10 piezoelectric bimorphs connected in parallel.

3.3. Fibre-Optic Shape Sensing

Wing shape changes influence the aerodynamics and are also considered a source of load acting on the wing. For load alleviation purposes and closed-loop control, shape sensing and wing deformation monitoring are necessary.

The wing contains a total of 14 optical fibres. Figure 5 shows the layout of the fibres that are bonded onto the skin and connected to the fibre connector hub. This layout was chosen to capture the morphing behaviour including bending and torsion. The six independent morphing modules and the wingspan structure contain two fibres each, one on the upper surface and one on the lower surface.

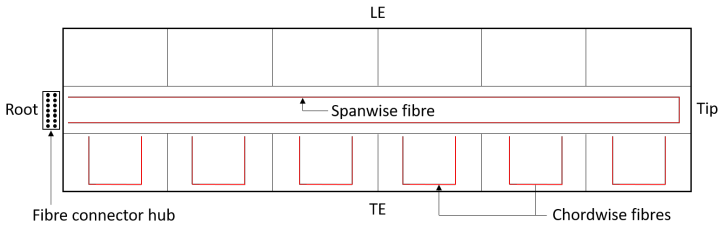

Figure 5. Layout of the spanwise and chordwise optical fibres (in red) on the SmartX wing. Connections to the 14 fibres are through the fibre connector hub.

A multi-modal fibre-optic principle is incorporated, which involves a combination of spectral sensing for local sensor measurement and interferometric sensing for measuring between sensor pairs. This sensing method was chosen to measure simultaneously at particular points as well as along given path lengths. This method also allows for capturing more data while keeping the number of fibre Bragg grating (FBG) sensors to a minimum.

Figure 6 shows the fibre layout and FBG location of one of the morphing modules. All the fibres on the wing are custom (Corning ZBL SMF-28e) single-mode fibres with FC/APC connectors and contain 4 FBG sensors each. The FBGs have high reflectivity (>84%) and bandwidth (>0.85 nm). Each grating is 3 mm long and operates in the C-band wavelength range (1530 nm–1565 nm). These parameters were particularly chosen to conform with the capabilities of the interrogators used.

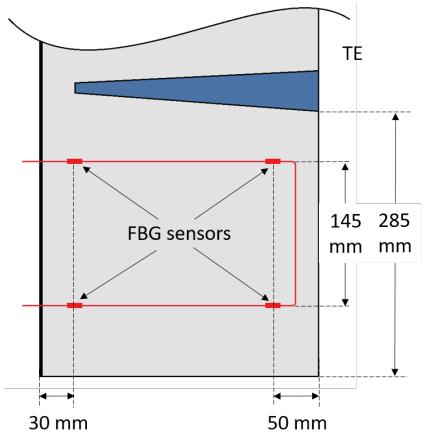

Figure 6. Location of the fibre (in red) and the FBG sensors on one of the morphing modules.

When the fibres, and in turn the gratings, are subjected to external mechanical (or thermal) perturbations, two optical changes are introduced that are vital for capturing the shape of the wing. The output of the first change gives the local strain measurement at the location of the grating measured by a spectral sensing interrogator. The second change gives the displacement between any two gratings measured by an interferometric sensing interrogator.

Each of the six morphing modules (and the wingspan) have a *U-shape* fibre layout parallel to the axis of bending and symmetric to their central axes (Figure 6). During bend up and bend down, the two fibres undergo similar loading, while during twisting one fibre experiences tension and the other experiences compression. The coupled motion of bending up, bending down, and twisting is analysed to interpret the morphing nature and to estimate the current shape of the wing surface. To determine the shape, the Optical Fibre Strain measurements are used by mapping them to the final deformed shape of each of the morphing sections. Such a mapping is calibrated by applying a selected number of morphing actuator settings and externally applied load while observing the resulting shape as well as the measured strains from the optical fibres. As the ZBL SMF-28e fibres are capable of withstanding larger deflections due to their high tensile strength, the actual limitations are set by the morphing and structural design.

The hybrid sensing approach also aims to reduce the overall costs by considerably reducing the cost of the fibres. This is realised by using the least number of gratings per fibre. Additional studies using this sensing approach have shown that the total number of fibres required can essentially be reduced to seven for the SmartX wing without compromising on the accuracy; i.e., one each for the six morphing modules [27] (chordwise) and one for the wing [28] (spanwise). In short, a single morphing surface requires just one fibre containing four FBG sensors [29]. Furthermore, once properly calibrated, this fibre-optic methodology is capable of identifying the position and magnitude of an external load acting on the morphing surfaces [30]. The data acquired can be integrated with the control loop for real-time feedback for load monitoring and load alleviation purposes. Details of the procedure and in-depth results can be found in Ref. [31].

3.4. Boundary Layer Sensor

Boundary layer sensors are installed to distinguish between various boundary layer states, which can be used for drag optimisation. Sixteen boundary layer sensors, relying on piezoelectric bimorphs, are embedded in the top skin of the SmartX wing. In this case, the bimorphs have a size of 3 mm width and 10 mm length and are operated in the direct piezoelectric mode (i.e., an experienced load results in an electrical signal). Using a 3D printer (Ultimaker 3, Ultimaker B.V., Utrecht, The Netherlands), a polylactic acid (PLA) box was 3D printed to house the piezoelectric bimorph sensors. About 2 mm of the piezoelectric bimorph length was clamped in one of the walls of this box, leaving a free length of 8 mm.

On the free end of the piezoelectric bimorph, a 3D-printed PLA vane was glued using cyanoacrylate adhesive. This vane later pierced the skin of the airfoil to mechanically couple the boundary layer to the piezoelectric bimorph. The vane reached a height of about 1.7 mm above the airfoil skin and had a width of 6.0 mm. A schematic representation of the piezoelectric bimorph including the vane inside the box is given in Figure 7. Under these boundary conditions, the natural frequency of the sensor was measured to be about 3 kHz in the direction of the flow.

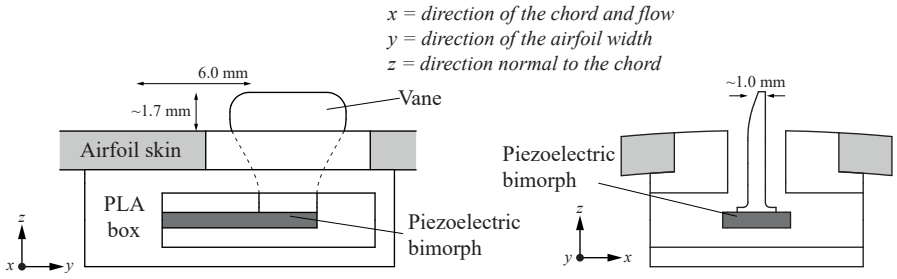

Figure 7. Schematic representation of a piezoelectric bimorph sensor mounted underneath the airfoil skin. The vane pierces the skin to transfer the oscillations from the boundary layer to the piezoelectric bimorph.

An ultra-low input current CMOS amplifier was directly connected to both outer electrodes of the piezoelectric bimorph, connecting the piezoelectric layers in series, providing a resistive load of 100 MΩ. The amplifier copies the voltage obtained from the piezoelectric bimorph, amplifies it, and drives a data acquisition unit without signal loss due to wiring and circuit load. To minimise the environmental noise, the wires between the piezoelectric bimorph and amplifier were taken as short as possible. The amplifiers were mounted on the bottom of the PLA box simply using double-sided tape, requiring only a couple of centimetres of wire between the bimorph and amplifier. To obtain as much information from the sensors as possible, frequencies up to the resonance frequency of 3 kHz have to be captured. This requires a sampling frequency of 6 kHz to prevent aliasing.

In total, 16 sensors are installed, divided into 2 rows of 8. This way, information on the local boundary layer state in both chord and span direction can be obtained. One row is positioned near the root of the wing, while the other is located near the tip, as shown in Figure 8. They are positioned so that the turbulent wedge created from one of the sensor vanes does not influence the measurement of any of the other sensors located downstream. The sensor boxes were mounted before the wing skins were joined together. The boxes were glued using epoxy resin in pre-drilled 9 mm holes on the inside of the top skin. The wires from the amplifiers were routed directly towards the leading edge through pre-drilled holes in the spars. They then move along the leading edge towards the root of the wing.

In the current configuration, the data of the 16 sensors sampled simultaneously are analysed offline using fast Fourier transforms. This allowed for the reconstruction of the location of laminar-to-turbulent transition to within 55 mm of the chord direction. Research towards more rapid data analysis is ongoing in order to be able to use the sensor signal as online input for the controller.

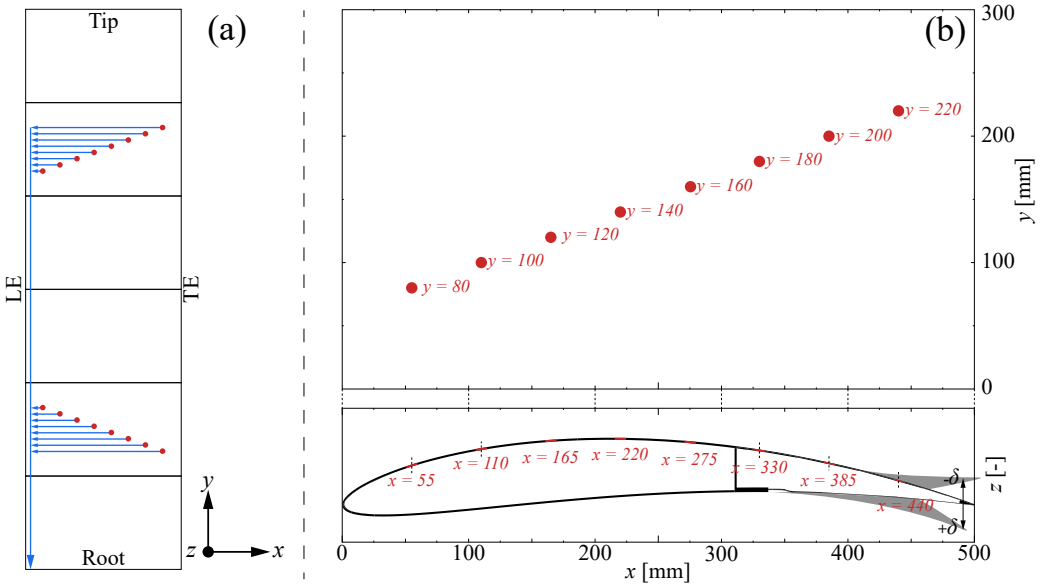

Figure 8. (**a**) Sensors locations (red circles) and wire paths (blue arrows) installed in the top skin of the SmartX wing. (**b**) Coordinates of sensors installed within a single section, including upper and lower morphing positions.

4. SmartX Technology Integration

To achieve the objectives outlined in Section 2, SmartX integrates several state-of-the-art technologies, which were explained in Section 3, into a hardware technology integrator capable of continuous autonomous control. This wing technology integrator, called the SmartX-Alpha, is composed of several closely integrated building blocks, as shown in Figure 9. The technology integration can be divided into several system-level segments:

1. Morphing module and actuator system integration: the slow and fast morphing concepts;
2. Sensor system integration: the fibre optics and the flow sensors;
3. Software and data integration: streamlining the acquired signals and fusing redundant and distributed sensor information into a hybrid output;
4. Control system integration: sensor data fusion and feedback to the morphing modules.

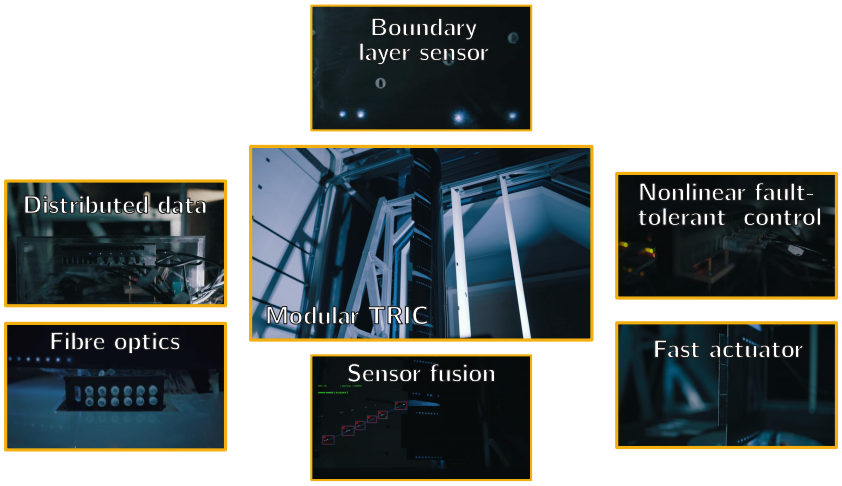

Figure 9. The SmartX integration blocks.

4.1. Morphing Module and Actuator System Integration

The SmartX technology integrator uses slow and fast morphing concepts, as described in Section 3. The arrangement of both morphing concepts is as follows. The TRIC morphing

modules are located at the trailing edge of the technology integrator while the fast morphing piezoelectric benders are mounted onto the trailing edge of the TRIC morphing modules. An overview of the design of the wing is presented in Figure 10 and described in more detail in Ref. [25].

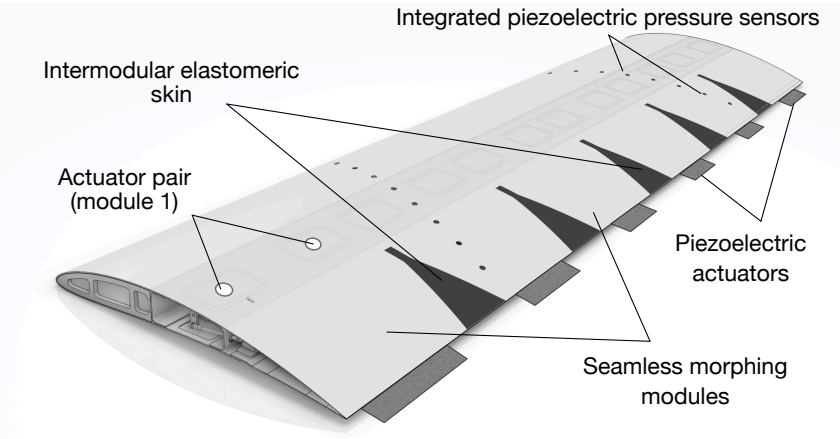

Figure 10. SmartX-Alpha sensor hardware integration.

4.2. Sensor System Integration

Next to the state-of-the-art sensor technologies described in Section 3, the wing was equipped with conventional strain gauges (for reference purposes only) and LEDs for a novel vision-based wing motion tracking system, as described in Refs. [32,33]. These sensors are integrated into the wing at the early stage of the manufacturing process. Figure 11 shows the integration of the components at the final stages of the manufacturing with two top and bottom wing halves exposed. The components are bonded with a thickened epoxy resin using cotton flocks and reinforced with a fibre-glass wrapped foam wedge. The cabling is routed from the trailing edge via the rear spar and exits the root either via the D-box or the wing-box. The actuator base, holding the servos, LEDs circuit and the piezoelectric boundary layer sensors are bonded on the upper skin. The fast morphing actuators were bonded to the bottom. The fibre optic sensors are bonded with a fast curing bonding compound to both upper and lower skins. Sufficient slack is given to ensure that the wiring and optical fibres do not restrict the motion of the morphing modules.

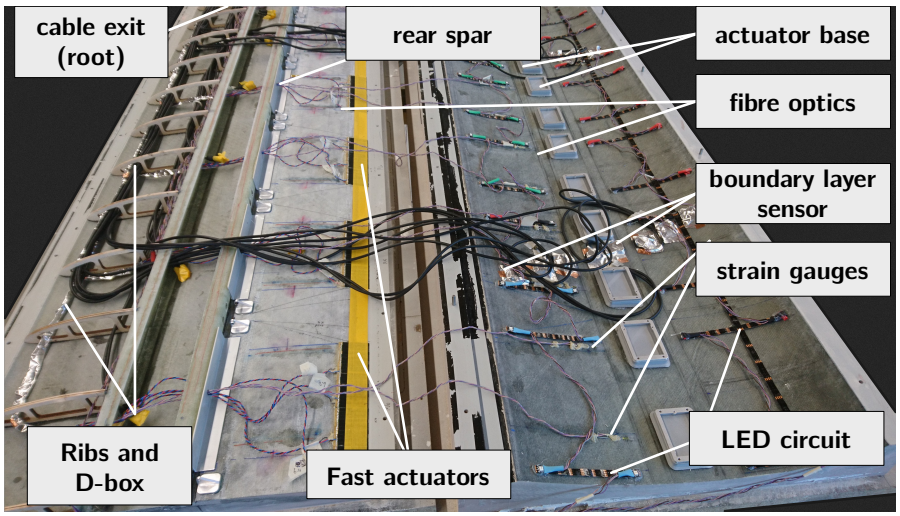

Figure 11. SmartX-Alpha sensor hardware integration and manufacturing.

4.3. Software and Data Integration

Due to its modular design and multi-actuation and multi-sensing capabilities, the number of sensors and actuators and their hardware controlling components increase with multiples for each module. To allow real-time control of numerous actuators and sensors, a distributed data-sharing architecture is developed. The structure allows parallel integration of hardware and software components. The software architecture is developed in C++ with the real-time D-SIM framework, connecting several PC nodes over a local Ethernet network. D-SIM is a framework written in C++, that facilitates the synchronisation of real-time variables over a distributed ethernet network. The resulting architecture allows integration in native C++ software components as well as standardised industry and academic software packages (LabView, MATLAB, Simulink). Various off-the-shelf boards and cards (microcontroller boards, digital-to-analogue converter (DAC) systems) and custom-built components (driver circuits, microcontroller units) can be integrated into the architecture.

4.4. Control System Integration

At the centre of the controller hardware are 12 servos commanding the morphing shapes of 6 trailing edge modules. These actuators are connected to an array of RS-485 devices communicating serially via the RS-485 protocol over a single physical USB bus updating to a D-SIM node. With the given RS-485 hardware configuration, the maximum achievable communication update rate was $\tilde{6}7$ Hz. The actuation angles of the servo are constrained to $\pm 25^{\circ}$ as to not exceed the physical limits of the system. The trailing edge fast morphing actuators are bundled into 19 sets of controllable actuator units requiring 2 logic level driver signals (0–5 V) each. These 38 signals are regulated by 3 micro-controllers boards equipped with Atmel 2560 Microcontroller. The driver signal is frequency modulated on the microcontroller, allowing for independent control of the oscillating frequency for each actuator. A Simulink program is integrated into the software architecture running the control law in real-time, with new control input updates entering at 200 Hz. An external balance system and integrated strain gauges allow for measuring the three-axes root reaction forces and moments required for the controller. The central control law consists of an Incremental Nonlinear Dynamic Inversion (INDI) with Quadratic Programming (QP) control allocation [34]. The incremental control was designed to guarantee robustness against model uncertainties, external disturbances, and fault tolerance in the event of actuator failure.

5. Results Overview

This section introduces the results that were obtained using the SmartX-Alpha wing demonstrator. A summary of the results will be shown and discussed here, and the reader is referred to the respective papers to get the details on the test setups and the boundary conditions and assumptions of the experiments.

Results are presented relating to the first two objectives of the SmartX project: (i) drag reduction in cruise and (ii) load control. No results have been obtained so far for the remaining two objectives: (iii) aeroelastic stability control and (iv) lift control. Prior to showing results related to the first two objectives of the SmartX project, the modal analysis properties of the SmartX-Alpha demonstrator are discussed.

5.1. Characterisation of the SmartX-Alpha Demonstrator

It is essential for a demonstrator that its mass and stiffness properties are known. The modal properties of the SmartX-Alpha demonstrator were obtained from a ground vibration test [35]. The modal results are summarised in Table 2.

Table 2. SmartX-Alpha demonstrator measured modal properties.

Mode	Frequency [Hz]	Damping [%]	Description
1	4.90	1.22	rigid body base out-of-plane displacement coupled with wing bending
2	5.76	0.70	first wing out-of-plane bending with free flaps, Figure 12a
3	18.40	0.90	second wing out-of-plane bending with rigid body base out-of-plane displacement Figure 12b
4/5	24.90/26.50	0.80/1.16	out-of-plane coupled to in-plane bending for/aft Figure 12c
6	27.60	1.22	first wing out-of-plane bending with inboard bending flaps
7	30.70	2.20	first wing torsion
8–15	34.00–60.00	-	flap modes Figure 12d

The lowest frequency mode is essentially a rigid body out-of-plane displacement mode. That mode does not have a 0 Hz frequency because the rigid body mode couples with the first wing bending mode. The involvement of the wing flexibility leads to a frequency of 4.90 Hz. The purely flexible first bending mode without rigid body motion is the second mode, which has a frequency of 5.76 Hz. The trailing edge flaps all move in phase. The next mode at 18.40 Hz is the second bending mode, which couples to the rigid body out-of-plane displacement mode. There is no second bending mode without a rigid body out-of-plane displacement, as was the case for the first bending mode. Then there are modes 4 and 5 with almost the same frequency, namely the coupled in-plane and out-of-plane bending modes. The reason why the two modes do not have the exact same frequency is because of the asymmetry in the wing's airfoil. Mode 6 exhibits the influence of the flexibility of the flaps, as the inboard flaps do not move as a rigid body but bend elastically. Mode 7 introduces wing torsion, typically a higher frequency mode than wing bending modes. However, it is remarkable that for the SmartX-Alpha wing demonstrator, the first torsion mode is only the seventh mode. The remaining modes 8 to 15 are all flap modes with different flap orientation distributions along the wing span.

Selected modes from Table 2 are shown in Figure 12. Various bending modes are shown to demonstrate the interaction between the wing bending and the flap motion, as well as the interaction between the in-plane and out-of-plane bending. Furthermore, only one out of eight flap modes is shown since they are similar and dominated by flap motion only.

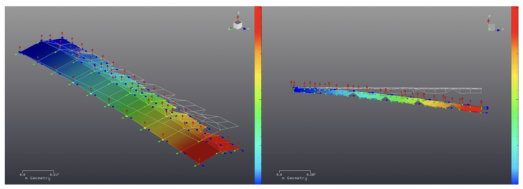

(**a**) Mode 2, 5.76 Hz

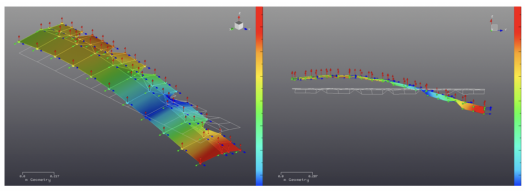

(**b**) Mode 3, 18.40 Hz

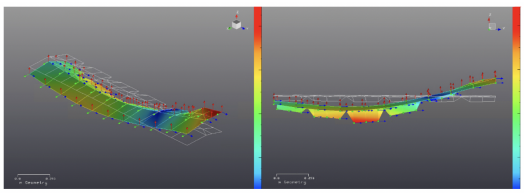

(**c**) Mode 4, 24.90 Hz

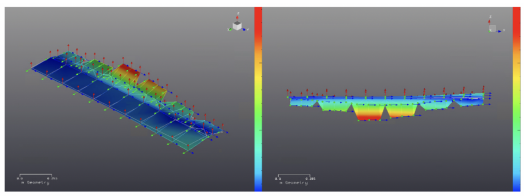

(**d**) Mode 8, 34.00 Hz

Figure 12. Four selected modes of the SmartX-Alpha wing demonstrator.

5.2. Drag Reduction Results

The effect of the SmartX-Alpha morphing flaps on the boundary layer transition point has been investigated experimentally using the technology explained in Section 3.4. The location of the boundary layer transition point is a measure for the wing viscous drag. A dedicated wind tunnel experiment was conceived for that purpose [36]. The chordwise transition point locations are shown in Figure 13. Results are shown for morphing flap number 2, which is located near the root of the wing, and morphing flap number 5, which is located outboard of the wing. The transition point x/c_{tr} is measured for various angles-of-attack α ranging from -4° to 12° and various flap settings δ ranging from -15 mm (upwards) to 15 mm (downwards) flap trailing edge vertical displacement.

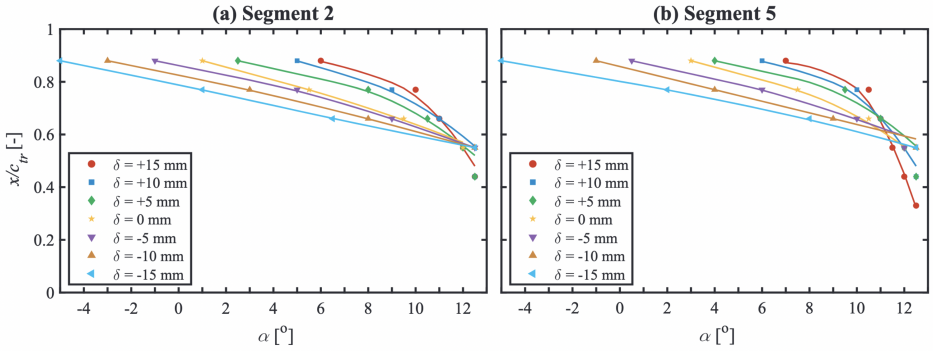

Figure 13. Location of the transition point versus angle-of-attack for various morphing flap settings for (**a**) flap segment 2 (inboard) and (**b**) flap segment 5 (outboard) [36].

The results of Figure 13 can be interpreted as follows. The transition point of segment 2 can be moved towards the trailing edge from approximately 75% of the chord to approximately 90% of the chord for a typical cruise angle-of-attack of 2°. This means that the wing has a larger laminar boundary layer region, which results in lower viscous drag. The effect is less pronounced for flap segment 5, but even there the transition point is moved from approximately 80% to approximately 90%. These results demonstrate that the morphing flap settings can indeed move the transition point downstream, actively reducing the wing drag in cruise. More detailed results and detailed discussions can be found in Ref. [36].

5.3. Load Control Results

Static or manoeuvre loads and dynamic or gust loads can be actively controlled using the morphing flaps. The gusts can have various lengths, depending on the aircraft's velocity, resulting in various frequencies. The larger the aircraft velocity, the higher the gust frequency. The frequency range of a gust for a transport aircraft is between 0.1 Hz and 10 Hz, as required by certification regulations. Manoeuvre loads are static and are expressed as g loads. A typical value for a transport aircraft is between -1 g and 2.5 g. The control strategy to mitigate the loads by redistributing them over the wing span is the Incremental Nonlinear Dynamic Inversion (INDI) method [37]. The method is adapted with quadratic programming control allocation augmented with virtual shape functions (INDI-QP-V) to smoothen the morphing wing deformations. The details of the experimental results presented below can be found in Ref. [38].

The gust load alleviation potential of a control system is dependent on the gust frequency because the interaction between the gust frequency and the wing eigenfrequencies determines the magnitude of the response. The load alleviation is expressed using the reduced wing root shear force F_y and the wing root bending moment M_x. These two quantities are a measure of the load intensity on the wing. This load intensity determines the stress level in the wing structure and hence the mass of the wing. Both the wing root shear force and the wing root bending moment can be alleviated up to 75% for the long gust of 0.5 Hz. The load alleviation potential was reduced to almost zero for the shorter

gusts of 4.5 Hz. This was attributed to phase lags in the control system due to the noise filters for the sensors.

The load alleviation case for 0.5 Hz is shown in Figure 14. The wing root shear force and bending moment results of the 0.5 Hz gust are investigated in open-loop and closed-loop. It is clear from the figure that the open-loop load peaks are reduced in closed-loop. An effect of the control law is that the closed-loop positive load peak is followed by a negative load peak, which is not present in the open-loop case. This poses no problem for the wing structural design as this negative peak does not impose an additional negative load because the wing is trimmed and is already exposed to a finite shear force in the undisturbed case. The actuator response is numbered from inboard to outboard, with *act1* being the most inboard actuator. Each of the six morphing flaps has two actuators. The actuator response shows no saturation, and the smoothness of the deformation pattern of the flaps can be observed. This is a consequence of the virtual shape function smoothing of the INDI-QP-V algorithm.

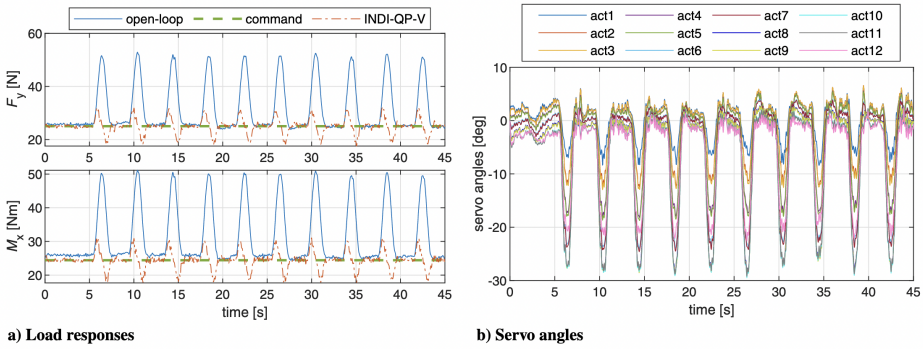

Figure 14. Dynamic load alleviation for (**a**) root shear force and root bending moment and (**b**) the required actuator settings for a 0.5 Hz gust [35,38].

Simultaneous gust and manoeuvre load alleviation leads to different results. It was demonstrated experimentally that over the entire gust frequency range, the wing root shear force could be reduced by 44% and the wing root bending moment by 45%. These values are lower compared to the long gust load reduction but higher compared to the short gust load reduction. This is because the manoeuvre loads dominate the load spectrum and are mainly sizing.

6. Summary and Conclusions

The present work shows that it is indeed possible to design and construct a wind tunnel model for an aircraft wing in which the following objectives are integrated simultaneously: (i) real-time drag reduction in cruise, (ii) static and dynamic load control, (iii) aeroelastic stability control, and (iv) lift control. The selected smart technologies to enable these simultaneous objectives were: (i) slow morphing control surfaces, (ii) fast morphing actuators, (iii) fibre-optic sensors, and (iv) piezoelectric flow sensors. The integration of the actuation and sensing is demonstrated, as well as the software and data fusion methods to make the sensor data of the over-sensed wing suitable for feedback control. The control methodology itself is also described in this paper.

Ground vibration tests of the SmartX-Alpha wind tunnel model showed that the first six modes are associated with wing bending, both in-plane and out-of-plane. The bending modes are mostly coupled with rigid body out-of-plane motion. The trailing edge flaps also contribute to the bending modes, either by rigid body motion or by bending. The seventh mode is the torsion mode, and the subsequent modes up to the 15th mode are flap modes.

Boundary layer transition point locations were obtained experimentally as a measure of the drag. The transition point could be moved downstream from 75% to 90% chord on the inboard part of the wing, and from 80% to 90% chord on the outboard part of the wing. The static and dynamic loads could be mitigated using morphing flaps that were actuated

by the Incremental Nonlinear Dynamic Inversion control algorithm. Dynamic loads only could be alleviated by 75% for long gusts but almost 0% for short guests due to phase lags in the control system. Simultaneous static and dynamic load alleviation led to a reduction of 45%.

Author Contributions: Conceptualization, T.M. and R.D.B.; methodology, T.M., V.S. and N.N.; investigation, T.M., V.S., N.N., X.W. and I.M.; writing—original draft preparation, R.D.B., T.M., V.S. and N.N.; writing—review and editing, S.v.d.Z., J.S. and R.G.; supervision, R.D.B., J.S., S.v.d.Z. and R.G.; project administration, R.D.B.; funding acquisition, R.D.B. and R.G. All authors have read and agreed to the published version of the manuscript.

Funding: This research was funded by Delft University of Technology, Faculty of Aerospace Engineering, Department Aerospace Structures and Materials.

Institutional Review Board Statement: Not applicable.

Informed Consent Statement: Not applicable.

Data Availability Statement: Not applicable.

Acknowledgments: The authors want to acknowledge Pim Groen, one of the initiators of the SmartX project and who passed away during the course of the project. The authors want to acknowledge Nisarg Thakrar for his support in the development and manufacturing of the SmartX wind tunnel model. The authors acknowledge the excellent manufacturing skills of Martin Weberschock at Weberschock Development in Gleichen, Germany, for the wing construction and component assembly. The authors want to acknowledge Ben Scheele for his invaluable help with the complicated electronics of the SmartX demonstrator. Finally, the Delft University of Technology, Faculty of Aerospace Engineering, Department of Aerospace Structures and Materials is greatly acknowledged for the financial support.

Conflicts of Interest: The authors declare no conflict of interest.

Abbreviations

The following abbreviations are used in this manuscript:

AAW	Active Aeroelastic Wing
AFW	Active Flexible Wing
CMOS	Complementary Metal Oxide Semiconductors
DAC	Digital Analogue Converter
DARPA	Defense Advanced Research Projects Agency
D-SIM	Distributed Energy System Integrator
FBG	Fibre Bragg Grating
FC/APC	Fixed Connection/Angled Physical Contact
FP	Framework Programme
INDI	Incremental Nonlinear Dynamic Inversion
LED	Light Emittting Diode
MOSFET	Metal Oxide Semi Conductor Field Effect Transistor
NASA	National Aeronautics and Space Administration
OJF	Open Jet Facility
PLA	Polylactic Acid
PZT	Lead Zirconate Titanate
QP	Quadratic Programming
SARISTU	Smart Intelligent Aircraft Structures
SMF	Single Mode Fibre
TRIC	Translation Induced Camber
TRL	Technology Readiness Level
VCCTEF	Variable Camber Continuous Trailing Edge Flap

References

1. Dimino, I.; Lecce, L.; Pecora, R. *Morphing Wing Technologies: Large Commercial Aircraft and Civil Helicopters*; Butterworth-Heinemann: Oxford, UK, 2017.
2. Perry, B., III; Cole, S.; Miller, G. A Summary of the Active Flexible Wing Program. *J. Aircr.* **1995**, *32*, 10–15. [CrossRef]
3. Bonnema, K.L.; Lokos, W.A. AFTI/F-111 mission adaptive wing flight test instrumentation overview. In Proceedings of the Instrumentation in the Aerospace Industry, Proceedings of the ISAAerospace Instrumentation Symposium, Orlando, FL, USA, 1–4 May, 1989, Volume 35, pp. 809–840.
4. Sanders, B.; Crowe, R.; Garcia, E. Defense advanced research projects agency—Smart materials and structures demonstration program overview. *J. Intell. Mater. Syst. Struct.* **2004**, *15*, 227–233. [CrossRef]
5. McGowan, A.M.R.; Horta, L.; Harrison, J.; Raney, D. Research Activities within NASA's Morphing Program. In Proceedings of the Research and Technology Agency, Albuquerque, NM, USA, 15–16 May 1999.
6. McGowan, A.M.R.; Washburn, A.E.; Horta, L.G.; Bryant, R.G.; Cox, D.E.; Siochi, E.J.; Padula, S.L.; Holloway, N.M. Recent results from NASA's Morphing Project. In Proceedings of the SPIE Conference on Smart Structures and Materials: Industrial and Commercial Applications of Smart Structures Technologies, San Diego, CA, USA, 9 July 2002.
7. De Gaspari, A.; Riccobene, L.; Ricci, S. Design, manufacturing and wind tunnel validation of a morphing compliant wing. *J. Aircr.* **2018**, *55*, 2313–2326. [CrossRef]
8. Ciarella, A.; Tsotskas, C.; Hahn, M.; Werter, N.; De Breuker, R.; Beaverstock, C.; Friswell, M.I.; Yang, Y.; Özgen, S.; Antoniadis, A.; et al. A Multi-Fidelity, Multi-Disciplinary Analysis and Optimization Framework for the Design of Morphing UAV Wing. In Proceedings of the 16th AIAA/ISSMO Multidisciplinary Analysis and Optimization Conference, Dallas, TX, USA, 22–26 June 2015.
9. Pfeiffer, H.; Wevers, M. The European Project "Aircraft Integrated Structural Health Assessment II". Innovation for Sustainable Aviation in a Global Environment. In Proceedings of the Sixth European Aeronautics Days, Madrid, Spain, 30 March–1 April 2012.
10. Wölcken, P.C.; Papadopoulos, M. *Smart Intelligent Aircraft Structures (SARISTU): Proceedings of the Final Project Conference*; Springer: Berlin/Heidelberg, Germany, 2015.
11. Gonzalez, P.J.; Guimaraes Neto, A.B.; Chaves Barbosa, G.; Bertolin, R.M.; Silvestre, F.J.; Cesnik, C.E.S. X-HALE autopilot with stability augmentation and shape control based on loop separation. In Proceedings of the International Forum on Aeroelasticity and Structural Dynamics, Como, Italy, 25–28 June 2017.
12. Hansen, J.H.; Duan, M.; Kolmanovsky, I.; Cesnik, C.E.S. Control Allocation for Maneuver and Gust Load Alleviation of Flexible Aircraft. In Proceedings of the AIAA SciTech 2020 Forum, Orlando, FL, USA, 6–10 January 2020.
13. De Gasprari, A.; Ricci, S.; Riccobene, L.; Scotti, A. Active Aeroelastic Control Over a Multisurface Wing: Modeling and Wind-Tunnel Testing. *AIAA J.* **2009**, *47*, 1995–2010. [CrossRef]
14. Ricci, S.; De Gaspari, A.; Fonte, F.; Riccobene, L.; Toffol, F.; Mantegazza, P.; Karpel, M.; Roizner, F.; Wiberman, R.; Weiss, M.; et al. Design and Wind Tunnel Test Validation of Gust Load Alleviation Systems. In Proceedings of the AIAA SciTech 2017 Forum, Grapevine, TX, USA, 9–13 January 2017.
15. Nguyen, N.T.; Precup, N.; Livne, E.; Urnes, J.S.; Dickey, E.; Nelson, C.; Chiew, J.; Rodriguez, D.L.; Ting, E.; Lebofsky, S. Wind Tunnel Investigation of a Flexible Wing High-Lift Configuration with a Variable Camber Continuous Trailing Edge Flap Design. In Proceedings of the AIAA AVIATION 2015 Forum, Dallas, TX, USA, 22–26 June 2015.
16. Popov, A.V.; Grigorie, L.T.; Botez, R.; Mamou, M.; Mebark, Y. Closed-Loop Control Validation of a Morphing Wing Using Wind Tunnel Tests. *J. Aircr.* **2010**, *47*, 1309–1317. [CrossRef]
17. Barbarino, S.; Bilgen, O.; Ajaj, R.M.; Friswell, M.I.; Inman, D.J. A review of morphing aircraft. *J. Intell. Mater. Syst. Struct.* **2011**, *22*, 823–877. [CrossRef]
18. Weisshaar, T.A. Morphing aircraft systems: historical perspectives and future challenges. *J. Aircr.* **2013**, *50*, 337–353. [CrossRef]
19. Sun, J.; Guan, Q.; Liu, Y.; Leng, J. Morphing aircraft based on smart materials and structures: A state-of-the-art review. *J. Intell. Mater. Syst. Struct.* **2016**, *27*, 2289–2312. [CrossRef]
20. Li, D.; Zhao, S.; Da Ronch, A.; Xiang, J.; Drofelnik, J.; Li, Y.; Zhang, L.; Wu, Y.; Kintscher, M.; Monner, H.P.; et al. A review of modelling and analysis of morphing wings. *Prog. Aerosp. Sci.* **2018**, *100*, 46–62.
21. Chopra, I. Review of state of art of smart structures and integrated systems. *AIAA J.* **2002**, *40*, 2145–2187. [CrossRef]
22. Loewy, R.G. Recent developments in smart structures with aeronautical applications. *Smart Mater. Struct.* **1997**, *6*, R11. [CrossRef]
23. Nguyen, N.; Lebofsky, S.; Ting, E.; Kaul, U.; Chaparro, D.; Urnes, J. Development of Variable Camber Continuous Trailing Edge Flap for Performance Adaptive Aeroelastic Wing. In *Proceedings of the SAE Technical Paper*; SAE International: Warrendale, PA, USA, 2015; number 2015-01-2565. [CrossRef]
24. *CS-25 Large Aeroplanes*; Technical report; European Union Aviation Safety Agency: Cologne, Germany, 2008.
25. Mkhoyan, T.; Thakrar, N.R.; De Breuker, R.; Sodja, J. Design of a Smart Morphing Wing Using Integrated and Distributed Trailing Edge Camber Morphing. In Proceedings of the ASME 2020 Conference on Smart Materials, Adaptive Structures and Intelligent Systems. American Society of Mechanical Engineers Digital Collection, Irvine, CA, USA, 14–16 September 2020.
26. Werter, N.P.; Sodja, J.; Spirlet, G.; De Breuker, R. Design and experiments of a warp induced camber and twist morphing leading and trailing edge device. In Proceedings of the 24th AIAA/AHS Adaptive Structures Conference, San Diego, CA, USA, 4–8 January 2016. [CrossRef]
27. Nazeer, N.; Groves, R.M.; Benedictus, R. Assessment of the Measurement Performance of the Multimodal Fibre Optic Shape Sensing Configuration for a Morphing Wing Section. *Sensors* **2022**, *22*, 2210. [CrossRef] [PubMed]

28. Nazeer, N.; Groves, R.M.; Benedictus, R. Simultaneous position and displacement sensing using two fibre Bragg grating sensors. *Proc. SPIE Smart Struct. + Nondestruct. Eval.* **2019**, *10970*, 109701Z–1–109701Z–8. [CrossRef]
29. Nazeer, N.; Wang, X.; Groves, R.M. Sensing, Actuation, and Control of the SmartX Prototype Morphing Wing in the Wind Tunnel. *Actuators* **2021**, *10*, 107. [CrossRef]
30. Nazeer, N.; Groves, R.M. Load Monitoring of a Cantilever Plate by a novel Multimodal Fibre Optic Sensing Configuration. *SN Appl. Sci.* **2021**, *3*, 1–17. [CrossRef]
31. Nazeer, N. Fibre Optic Shape Sensing and Load Monitoring of Adaptive Aerospace Structures. Ph.D. Thesis, Delft University of Technology, Delft, The Netherlands, 2022.
32. Mkhoyan, T.; de Visser, C.C.; De Breuker, R. Adaptive Real-Time Clustering Method for Dynamic Visual Tracking of Very Flexible Wings. *J. Aerosp. Inf. Syst.* **2021**, *18*, 58–79. [CrossRef]
33. Mkhoyan, T.; de Visser, C.C.; De Breuker, R. Adaptive State Estimation and Real-Time tracking of Aeroelastic Wings with Augmented Kalman filter and Kernelized Correlation Filter. In Proceedings of the AIAA SciTech Forum, Online event, 11–15 & 19–21 January 2021. [CrossRef]
34. Wang, X.; Van Kampen, E.; Chu, Q.; De Breuker, R. Flexible aircraft gust load alleviation with incremental nonlinear dynamic inversion. *J. Guid. Control. Dyn.* **2019**, *42*, 1519–1536. [CrossRef]
35. Mkhoyan, T. Autonomous Smart Morphing Wing: Development, Realisation and Validation. Ph.D. Thesis, Delft University of Technology, Delft, The Netherlands, 2022.
36. Stuber, V. Piezo-sensors for in-situ boundary layer monitoring on morphing wings: Development, validation and implementation. Ph.D. Thesis, Delft University of Technology, Delft, The Netherlands, 2021.
37. Sieberling, S.; Chu, Q.; Mulder, J. Robust Flight Control Using Incremental Nonlinear Dynamic Inversion and Angular Acceleration Prediction. *J. Guid. Control. Dyn.* **2010**, *33*, 1732–1742. [CrossRef]
38. Wang, X.; Mkhoyan, T.; Mkhoyan, I.; De Breuker, R. Seamless Active Morphing Wing Simultaneous Gust and Maneuver Load Alleviation. *J. Guid. Control. Dyn.* **2021**, *44*, 1649–1662. [CrossRef]